Intra- and inter-operator repeatability of myocardial blood flow and myocardial flow reserve measurements using Rubidium-82 PET and a highly automated analysis program

[1,2]Ran Klein, M.A.Sc; [1]Jennifer M. Renaud, M.Sc; [1]Maria C. Ziadi, M.D.; [1]Stephanie L. Thorn, M.Sc; [3]Andy Adler, Ph.D.; [1]Robert S. Beanlands, M.D.; [1]Robert A. deKemp, Ph.D., P.Eng., P.Phys.

1. University of Ottawa Heart Institute, National Cardiac PET Centre, Ottawa, Ontario, Canada
2. University of Ottawa, School of Information Technology and Engineering, Ottawa, Ontario, Canada
3. Carleton University, Systems and Computer Engineering, Ottawa, Ontario, Canada

Author Contribution:
Ran Klein – Study design, methods implementation, data analysis, primary author
Jennifer M. Renaud – Major contributions to methodology and secondary author
Maria C. Ziadi – Operator 2
Stephanie L. Thorn – Operator 1
Andy Adler – Co-supervisor for Ran Klein, revising of manuscript
Robert S. Beanlands – Head of Cardiac PET Centre producing data and patient recruitment, final approval of manuscript for submission
Robert A. deKemp – Study conception and design, supervisor for Ran Klein, and senior author, editing of manuscript for submission

Corresponding Author: Robert deKemp
Head Imaging Physicist
Cardiac PET Centre
40 Ruskin St., Ottawa, Ontario, K1Y 4W7, Canada
Tel: +1-613-761-4275
Fax: +1-613-761-5406
radekemp@ottawaheart.ca

Word Count: 4569

Key Words: PET, rubidium-82, image processing, coronary blood flow, operator repeatability

Abstract

Background: Changes in myocardial blood flow between rest and stress states are commonly used to diagnose coronary artery disease. Relative myocardial perfusion imaging (MPI) is used routinely while myocardial blood flow quantification (MBF) may improve the sensitivity for detection of early disease. The ratio of flow at stress and rest (S/R) and their difference (S-R) have both been proposed as a means to detect regions with reduced myocardial flow reserve (MFR). In this study we describe a highly automated method to calculate regional and global rest, stress, S/R, and S-R polar maps of the left ventricle myocardium. **Methods:** We measured the inter- and intra-operator variability using two randomized datasets (n=30 each) for each of 2 operators (novice and expert) with correlation and Bland-Altman reproducibility coefficient (RPC%) analyses. **Results:** S-R MBF had less inter-operator dependent variability than S/R (RPC%= 5.0% vs. 12.6%, p<0.001). While there was no difference in intra-operator variability with S-R MBF (novice vs. expert RPC%=6.4% vs. 5.9%, p=n.s.), variability was higher in the novice-operator for S/R (RPC%=16.8% vs 8.5% respectively, p<0.001), suggesting that S-R may be preferred for detecting small changes in MFR. The novice operator's intervention pattern became more similar to that of the expert in the later dataset, emphasizing the need for adequate training and quality assurance **Conclusion:** The proposed method results in low operator-dependent variability, suitable for routine use.

Background

Coronary artery disease (CAD) is the leading cause of death worldwide [1-3]. Relative myocardial perfusion imaging (MPI) is a well-established technique for the diagnosis and prognostication of CAD. Assessment of absolute myocardial blood flow (MBF) and myocardial flow reserve (MFR; the ratio of stress to rest MBF) using dynamic PET may represent a more sensitive tool to detect multi-vessel disease [4-8] as well as sub-clinical CAD [9-11]. It has been proposed that the difference between MBF at stress and rest may be more suitable for detection of CAD [6,12]. PET MPI has been shown to yield prognostic value for the prediction of adverse patient outcomes [13-15], but quantitative analysis has been limited mainly to research applications [16]. Recent advances in PET instrumentation [17] and tracer availability may facilitate the routine application of flow quantification in clinical practice.

Our group and others have demonstrated that MBF can be measured accurately using ^{82}Rb PET[18,19] and that standard MPI with ^{82}Rb PET is cost-effective compared to ^{99m}Tc SPECT[20]. Instead of relying on an onsite cyclotron to produce short-lived PET tracers such as ^{15}O-water, ^{13}N-ammonia, or ^{11}C-acetate, a ^{82}Sr/^{82}Rb generator may be used as a source of ^{82}Rb for a 4-8 week period [21]. During the life of the generator, ^{82}Rb may be infused as frequently as every ten minutes, enabling fast serial imaging and high patient throughput. We developed a custom ^{82}Rb infuser to deliver a reproducible infusion profile regardless of the age of the generator, which may improve the reproducibility of MBF quantification [22,23]. The infuser also flushes the injection line automatically at the end of the infusion to remove activity outside the scanner field of view, which is important with the industry's transition from 2D to 3D PET instrumentation [24,25].

The accuracy of MBF and MFR quantification with PET has been validated in animal studies using micro-spheres [5,13,26-29] or other invasive measurements [4]. In humans, accuracy has been measured through agreement of MBF quantification using different PET tracers [18,30,31]. High precision is important for detection of serial changes during disease progression or therapy [11,32] and is evaluated through test-retest reproducibility [19,29,31,33-38], of which operator-dependent variability [30,33,39-42] is an important factor [43]. However, there are few reports of reproducibility of MBF quantification using ^{82}Rb PET [30].

Several software packages with the ability to quantify MBF from cardiac PET images have recently become available [30,39,44]. We developed a highly automated image processing workflow, expected to reduced operator variability in MBF quantification by minimizing user interactions [43,45]. We have previously evaluated the accuracy of this method for quantification of MBF using ^{82}Rb PET [18]. In this work we present a detailed description of our image processing workflow, and assess the inter-operator and intra-operator variability of our methodology for quantification of MBF, flow reserve, and flow differences using ^{82}Rb PET. Likewise, we evaluate the operator dependent variability for MPI, which is referred to as relative uptake in this study.

Methods and Materials

Patient Cohort

Thirty consecutive clinical patients that underwent a rest-stress ^{82}Rb perfusion scan at the University of Ottawa Heart Institute, National Cardiac PET Centre, between the 15th and 26th of June, 2009 were selected. All patients gave informed consent under a cardiac PET registry study approved by the Ottawa Heart Institute Research Ethics Board. Patients were instructed to abstain from caffeine intake for 12 hours prior to the exam, beta-blockers for 24 hours, and fast for at least 4 hours.

Image Acquisition

Scans were acquired according to our standard clinical protocol (Fig.1). Following a scout scan for patient positioning, a low-dose (0.5 mSv) fast CT scan was performed for attenuation correction of the rest data. ^{82}Rb (10 MBq/kg) was administered intravenously using a custom infusion system [22] over a 30 s interval to limit the

coincidence deadtime to <35% and to ensure accurate measurement of the bolus first-pass activity [23]. Dynamic data were acquired in 3D mode using a Discovery RX PET-VCT scanner (GE Healthcare, Waukeshaw, MI), and images of activity concentration were reconstructed using Fourier rebinning and filtered backprojection with a 12 mm Hann filter, into 15 time frames (10s × 9, 30s × 3, 60s × 1, 120s × 1, 240s × 1).

Dipyridamole (0.14 mg/kg/min) was infused for 5 min, and ^{82}Rb imaging initiated 3 min later following the same protocol used at rest. A second low-dose CT scan was then performed for attenuation correction of the stress ^{82}Rb data.

Image Analysis

Images were processed using an in-house software program (FlowQuant, Ottawa, Canada) developed for quantification of cardiac molecular function using a variety of tracers and in different species. The rest-stress workflow started with processing of the rest scan, continued with a nearly identical process for the stress scan, and ended with the stress-rest flow reserve analysis (Fig. 2).

Volume Reorientation

Uptake images were generated by averaging the last 5 time frames (8 minutes) to maintain high myocardium:blood pool contrast and reduce image noise. The uptake images were automatically processed to detect the location, orientation, and size of the LV myocardium (Fig. 3a,b). Ellipses were fit to the myocardial data in 3 orthogonal planes in an evolving reference frame. The benefits of working with 2D planes rather than the full 3D volume are reduced computational complexity and the ability of the operator to supervise the process and intervene as needed. The process was fully visualized using the reorientation graphical user interface (GUI) shown in Fig. 3c.

The LV processing began with automatic selection of a transverse plane intersecting the LV. In this transverse plane, the LV position was estimated using the center of mass of the pixel intensities. A full ellipse was then optimized to correlate with the uptake image as follows. A cost function maximized the correlation between the region overlapping a partial ellipse and its neighbourhood, by modifying five free parameters (x and y translation, ellipse rotation, and two ellipse dimensions (*a* and *b* in Fig. 3b). A mid vertical-long-axis (mid-VLA) image was created orthogonal to the transverse plane, along the estimated long-axis. A partial ellipse (4/3 of the long axis) was optimized in a similar manner with initial estimates of the ellipse location and dimensions derived from the previous stage. In theory, the LV orientation and position should be completely measured at this point, but a third orthogonal image along the mid horizontal-long-axis (mid-HLA) plane was also processed to further optimize the transverse rotation.

For quality assurance (QA) purposes a fourth orthogonal, short-axis (basal-SA) image was displayed, which should have a circular pattern centered on the long axis, shown with cross-hairs in Figure 3c. For further validation the operator could toggle the display to view a mid-ventricle-SA image.

For the rest scans, the initial parameter estimates at each orientation stage were based on characteristic values for the species type (human in this case). For stress scans, the LV myocardium size (ellipse dimensions) and orientation (angles) were presumed to be fixed and equal to those of the rest scan, but the positions could change. The LV position in the rest image was used as an initial estimate of the LV position in the stress image.

The graphical report (Fig. 3c) displays the results of the optimization process, which also enabled the operator to intervene at each stage if necessary by manual adjustment of the fitted ellipses. Automated processing would continue from the point of intervention to minimize operator bias on the final results. If no operator intervention was performed, then the reorientation process was fully automated as described. Any operator interaction was labelled on the report for retrospective QA.

LV and Blood Pool Segmentation

The transverse uptake images were reoriented to form 20 standard SA slices from apex to base, plus 3 slices beyond the apex and 3 slices past the base (in the atrium), thus the SA slice thickness was determined by the total long axis extent (4/3 *a)*. The SA pixel dimensions were unchanged from those of the original image.

The reoriented SA volume was sampled in a combined conical and planar coordinate system to generate a combined series of LV slices as shown in Fig. 4. The first 9 slices relate to the conical sampling of the apex, while the remaining 15 slices are SA planes from apex to atrium. The slice planes are superimposed (white dashed lines) on the VLA and HLA images in the right hand side. This coordinate system was used to define myocardial sample points at fixed (10°) angular intervals according to their radial distance from the LV long axis. Rather than fitting each point individually, a spline model was used to optimize the radii of 4 control points (at 90° intervals) in 3 slices (LV cavity, base, and atrium), as well as one control point at the apex as shown in Figure 4. For the rest scans, initial estimates of the spline points were based on the ellipse sizes determined in the reorientation stage. For the stress scans, the spline points from the rest scan were used as initial estimates. Having a spline model with only 13 degrees of freedom afforded fast execution of the optimization algorithm (Appendix A) as well as simple operator intervention. For quality assurance, the operator could monitor the automated sampling and intervene as needed by manipulating the radial position of the spline control points.

The myocardial radii determined from the spline model (36 points per slice x 24 slices= 864 points) were each shifted to the local maximum intensity position to account for regional shape variations. Local smoothness was enforced using a 2D median filter of the myocardial radii. Myocardial uptake values were averaged within regions of interest with specified endo- and epi-cardial extent (4 mm thickness) centered on the 864 LV sample points.

The sampled uptake activity was viewed as a polar-map and as a 3D model for quality assurance of the segmented LV shape, as demonstrated in Fig.5. For subsequent analysis in this study the LV polar map was considered as the inner 16 of 24 slices, which excludes the membranous septum and some of the lateral wall.

The standard 17 segment model was applied and segments were averaged according to ASNC guidelines [46] into 3 vascular territories corresponding to the major coronary arteries: left anterior descending (LAD) artery, left circumflex (LCX) artery, and right coronary artery (RCA). Segments were averaged to report regional tracer uptake corresponding to the vascular territories.

Three blood regions of interest were placed automatically in the LV cavity (C), base (B), and left atrium (A) as shown on the VLA and HLA images in Fig. 4. The extent of each region was predefined for each given species (8 mm in humans), and their length was 4 SA slices each. The regions were shifted in each SA plane to center the ROI in the cavity and maximize the distance from the myocardium, to minimize myocardial spillover into the blood region.

TAC Sampling

The sampling points from the registration stage were applied to all of the time frames of the dynamic image sequence to generate time-activity-curves (TAC). In the myocardium, a TAC, $C_{meas}(t)$, was generated for each sample point resulting in 864 TACs (36×24 rings). In the blood, three TACs were generated for the cavity, base, and atrium blood pool regions. In order to reduce noise, the median of the three blood region TACs was used as a blood input function for tracer kinetic modelling (Fig. 6).

Kinetic Modeling

The last stage in the processing of each scan was to solve the parameters of a kinetic model, based on the blood (input) and myocardium (output) TAC functions. Each polar map sector of the LV myocardium (apex to base plane) was optimized separately resulting in 36×16=576 sets of kinetic parameters (Fig. 7).

The uptake rate of ^{82}Rb, K_1 ml/min/g, was quantified using a one-compartment constant distribution volume (DV) model [47] at both rest and stress states:

$$C_m(t) = K_1 e^{-\left(\frac{K_1}{DV}\right)t} \otimes C_a(t)$$
(1)

$C_m(t)$ represents the modeled myocardial activity concentration, $C_a(t)$ is the measured arterial blood concentration as a function of time, t. In the DV model, DV is the ratio of the tissue and blood tracer concentrations when the compartments have reached a state of equilibrium. Since the net exchange of tracer is zero at equilibrium, DV can be expressed as:

$$DV = \frac{K_1}{k_2}$$
(2)

To further simplify the kinetic model, DV was set to a scan-specific, constant value determined by fitting the unconstrained model to the region of normal uptake in the polar map.

K_1 was related to flow, MBF ml/min/g, through $K_1 = MBF \times E(MBF)$, where

$$E(MBF) = 1 - e^{-PS(MBF)/MBF}$$
(3)

$E(MBF)$ is a model-specific extraction fraction that accounts for non-linear tracer extraction as a function of MBF and the effective permeability x surface-area product, PS ml/min/g [48,49]. This model is consistent with the observation that tracer extraction typically decreases with flow, despite the PS product increasing due to capillary recruitment. The following PS function was used, as determined previously in human subjects [18]:

$$PS(MBF) = 0.63 + 0.26MBF$$
(4)

The measured myocardial image concentration in each polar map sector, $C_{meas}(t)$, was estimated according to:

$$C_{model}(t) = TBV \cdot C_a(t) + (1 - TBV)C_m(t)$$
(5)

where TBV was the estimated total blood volume and (1-TBV) corrected for regional partial-volume loss in the myocardium [7].

The example in Fig. 7 shows a report for the kinetic modeling stage consisting of polar-maps of kinetic modeling parameters, K_1, k_2, and TBV. The DV estimate is included in the title. In addition, goodness–of-fit parameters (χ^2, R^2, the optimization convergence flag, and whether any of the parameters hit their upper bounds) are displayed in polar-map format to indicate regional reliability of the kinetic parameters. Finally, MBF (flow) and the uptake polar-maps are shown. Regional correspondence between uptake and flow patterns is expected.

The blood TAC (red line) and the mean sampled myocardium TAC in the high-uptake (>75% of maximum) regions (blue dots) are shown in the bottom panel of the figure. The partial-volume corrected myocardial TAC, $C_m(t)$, (cyan) and modeled-determined TAC, $C_{model}(t)$, (blue line) are also included together with the sampled myocardial TAC, $C_{meas}(t)$, (blue dots). The error between sampled and modeled myocardium TACs (green) shows little error and no temporal pattern, also indicating a good fit. The model fits and TAC data can also be viewed for any polar map sector with an interactive cursor selection.

Relative Uptake and MFR Analysis

The rest and stress scans were compared to analyze changes between states using the relative uptake and absolute flow polar maps. Each report included rest, stress, stress/rest, and stress-rest polar maps (corresponding to rest MBF, stress MBF, MFR, and ΔMBF for absolute flow), as demonstrated in Fig. 8. The polar maps were then segmented into the three vascular territories [46] to produce regional average values. Global average values were also calculated by averaging the same polar maps over the entire LV.

Inter- and Intra-Operator Variability

All patients were anonymized and copied in random order for repeat analysis by 2 operators. All scans were first processed automatically (with no operator intervention) from the orientation phase through to the kinetic modeling and MFR analysis.

The processed studies were reviewed independently by two operators, one novice (operator 1) and one expert (operator 2). The novice user had never used FlowQuant or any other software for quantifying cardiac function from images, while the expert user had used FlowQuant for over 1 year to review and process hundreds of clinical studies. Both operators were instructed on use of the FlowQuant program and methods for quality assurance review of the automatically processed results, using a separate dataset which is not included in this work.

The operators reviewed the QA reports (Figures 3-8) saved during the reorientation, LV segmentation, and kinetic modeling steps, and reprocessed with manual intervention, any scan that was considered suboptimal. Thus, each scan was processed four times (twice by each operator). Specifically, processing was considered to be suboptimal in cases where: 1) the ellipse did not properly track the myocardium in the LV orientation phase; 2) the sampling points did not properly overlay the myocardium in the LV segmentation step due to the presence of adjacent organ activity ; 3) there was discordance between the TACs for the cavity, base and atrium blood regions; 4) there was discordance between the patterns of relative uptake and absolute MBF polar maps in the kinetic modeling phase; 5) the goodness-of-fit parameters indicated suboptimal fitting of the kinetic model to the measured data, i.e. non-uniform R^2, high χ^2 values, or a non-random distribution of the residuals.

The operators were instructed to correct these issues by first ensuring accurate ellipse placement during reprocessing, but intervening as little as possible. This could be accomplished by first changing the transaxial plane to choose an image with optimal contrast between the myocardium and the background and/or cropping the inferior slices to remove adjacent organ activity. The operator could also intervene on the subsequent VLA and HLA slices by properly resizing and repositioning the ellipse over the myocardium, if needed. In the LV segmentation phase the operator could adjust the spline control points to improve overlap of the model contour with the myocardium uptake.

The reprocessed datasets were analyzed for inter- and intra-operator variability in rest, stress, stress/rest and stress-rest both in relative uptake and absolute flow. The analysis was performed in the three vascular territories as well as globally. For intra-operator agreement the two datasets processed by each operator were compared with one another, and the results for each operator were reported separately. For inter-operator agreement, the repeated analyses were combined and then compared between operators.

Statistical Analysis

Agreement between paired datasets was visualized using correlation analysis and a linear regression fit. Pearson's correlation (r^2) was used to report agreement between datasets. Fisher's z-transform was used to calculate the probability of two r values being significantly different. In addition, a Bonferroni correction was applied for multiple comparisons.

Differences between datasets were analyzed using Bland-Altman plots [50] and a reproducibility coefficient (RPC), calculated as 1.96 times the standard deviation of the differences. Thus 5% of the data points are expected to fall outside the range of mean ± RPC, assuming the differences follow a Gaussian distribution. RPC values were compared by conversion to variance ($\sigma^2=(RPC/1.96)^2$) and then applying an f-test with p<0.05 considered significant. In addition the %RPC was reported as the ratio (%) of the mean rest, mean stress, mean stress/rest, and mean rest and stress for rest, stress, stress/rest, and stress-rest respectively. Likewise, biases were evaluated as the mean of differences between datasets and were reported as the ratio (%) of the bias scaled in the same way as %RPC.

Group mean and variance differences were evaluated using a two-sided student t-test and F-test respectively with Bonferroni correction and $p<0.05$ considered significant.

Results

Patient Demographics

Patient demographics are summarized in Table 1. The youngest and oldest volunteers were 32 and 81 years of age respectively. The mean±sd global MBF, MFR, and ΔMBF are listed for all 4 datasets (2 operators × 2 repeated datasets), No significant differences in means or variance were found between or within operator's repeated datasets ($p>0.05$).

Operator Intervention

Operator intervention at each processing stage is summarized in Table 2. The intervention of Operator 2 remained consistent between datasets when compared to operator 1. Both operators intervened primarily by cropping adjacent organ activity on the inferior image. Operator 1 cropped 18 images in the first analysis but only 6 in the second analysis, which was more similar to the interventions of operator 2. This suggests some improvement of processing skills as operator 1 gained experience with the software, with less intervention required in the second analysis.

Inter-operator Variability

Relative uptake and absolute flow inter-operator analyses are shown in Fig. 9 and Fig.10 respectively. Both figures contain correlation and Bland-Altman plots for rest (bottom left), stress (top left), stress/rest, (top right), and stress-rest (bottom right) using the data from the three vascular territories. Overall, excellent correlation, and low bias, was demonstrated both for relative uptake and absolute flow. In all cases the slope was close to unity (0.956-1.04) and the intercept was within ±5% of the mean values.

Bias(%), correlation (r^2), and RPC(%) values are summarized in Fig. 11, Fig. 12, and Fig. 13 respectively. While, relative uptake appears to have lower bias than absolute flow, none of the bias values significantly differed from zero (p>n.s.). All inter-operator correlations were higher for absolute flow compared to relative uptake, but were significant only in the case of rest and stress-rest ($p<0.05$). Finally, the reproducibility coefficients for relative uptake, were all lower (more reproducible) than for absolute flow ($p<0.001$).

Intra-Operator Variability

Intra-operator biases were also larger with absolute flow compared to relative flow ($p<0.001$). None of the biases were significantly greater than zero (p>n.s.) as with the inter-operator biases. In all cases correlation was excellent ($r^2 \geq 0.97$).

Generally, intra-operator 2 (expert) had significantly higher correlations ($p<0.001$) and lower RPC% ($p<0.001$) for rest, stress, stress/rest and stress-rest than intra-operator 1 (novice), as shown in Fig. 12 and Fig. 13 respectively. Interestingly, only absolute flow stress-rest correlation (p=0.6) and RPC% (p=0.4) did not significantly differ between operators. These results may suggest better intra-operator reproducibility with experience, and that absolute stress-rest may be more robust against operator dependent variability.

Regional Variability

The inter- and intra-operator RPC% for absolute flow values (combined rest and stress) in the three vascular territories and globally are listed in Table 3. RPC in absolute units is also presented as 95% confidence intervals that could be used in serial comparisons that account for operator variability. The results suggest that the LCX region may be less sensitive to operator interaction than the LAD and RCA regions, but the general agreement remains very

good, with 95% of disagreements being below 6.1% (0.095 ml/min/g) in the territory with largest variation for intra-operator 1.

Discussion

In this work we assessed the inter- and intra-operator variability of relative uptake and absolute flow measurements in rest, stress, stress/rest, and stress-rest using the FlowQuant software program with two operators and two identical, anonymized, and randomized sets of images. Operator 2 was an experienced user whereas operator 1 was a novice. Operator 1 was trained on a small, separate set of images and was then left to process the data independently. By measuring the variability with expert and novice users we can better define the range of operator variability.

It is possible that the difference in user interactions (Table 2) between datasets 1 and 2 corresponds to operator 1's learning curve. As experience was gained by the operator, less intervention was required. Thus operators 1 and 2 form a worst and best case scenario respectively. While the intra-operator agreement of operator 1 remained consistently lower than that of operator 2, both the inter- and intra-operator metrics illustrated excellent agreement.

One patient scan, with the largest intra-operator discordance in MBF values, is exemplified in Fig. 14. In this rest scan the operator neglected to intervene during reorientation in dataset 1 (left), but did intervene in the dataset 2 (right), resulting in an improved fit of the ellipse in the mid-VLA and mid-HLA slices. The largest discordances were in the inferior wall and the apex, corresponding to the RCA and LAD territories (not shown). The RCA and LAD data points associated with the dataset 1 are shown in the inter-operator rest, stress/rest, and stress-rest Bland-Altman plots in Fig. 10 using filled blocks. Since the rest orientations and ellipse sizes were applied to the stress scans (not shown), the MBF stress/rest and stress-rest polar maps had similar, but shifted, spatial patterns (Fig. 14), and varied in scale due to different blood sampling. In a clinical setting, it is expected that this registration error would be identified as part of the QA process and that the image would not be interpreted until reprocessed. The importance of the saved graphical reports and their routine review is thus emphasized.

Comparison to other repeatability studies

Previous studies have evaluated operator dependent variability of MBF and MFR with other software programs. The results of some of these studies are listed in Table 4 alongside the results of this study. While the methodology of each study is slightly different, it is reassuring that our proposed method performs similarly or better in most cases. The work of El Fahkri et al. [30] used the average across 4 datasets per operator to measure inter-operator variability. Reproducibility across averages is expected to result in higher correlations and lower RPC compared with the standard methodology used in the present study. Comparison of correlations is further complicated since inter and intra-operator correlation coefficients varied considerably. In addition, some of the correlations were reported using a Spearman non-parametric correlation coefficient (ρ) and some were reported using a Pearson correlation coefficient (as performed in this study) which is more sensitive to outliers.

The work of Knešaurek at al. [40] used the PMOD software, which requires manual operator interaction, and may explain the increased operator variability at stress. It is not clear in this paper if both sets of data were processed by the same operator or two different operators (we assume the former).

Schindler et al. [41] measured inter-operator agreement at rest, CPT, and stress. While the rest and stress results are included in Table 4, the CPT results (r^2=0.61, RPC=26%) were excluded for simplicity. In addition, while Schindler et al. make reference to intra-operator variability, these were performed on separate, repeat scans, and thus include variability resulting from changes in the subject between scans, as well as variability in the imaging process. In Sawada et al. [33] and El Fakhri et al. [31] repeat measurement agreements were also reported, and referred to as inter-study variability and reproducibility respectively.

Nestrov *et al.* [39] measured inter- and intra-operator variability at rest and stress in 10 patients using 4 operators with various degrees of experience. Each operator processed the data twice at two-week intervals. Analysis included global, 4 coronary artery territories (apex was isolated from the LAD territory), and 17 segments. Variability increased with the number of segments (inverse to ROI sizes) likely due to increases in noise and physiological MBF heterogeneity [51,52]. Since the segmental and regional analysis was performed using interclass correlation coefficients we could not directly compare all Pearson correlation coefficients. However, comparison of RPC% values was possible, and showed less variability with our method.

The operator dependent variability in our study is similar or lower than previously published methods, even when including the results of a novice operator. Thus the results suggest that a highly automated approach with minimal operator intervention is robust against operator induced variability.

Relative Uptake vs. Absolute Flow

The results demonstrated better reproducibility of relative uptake through lower biases and lower RPC compared to absolute uptake, while correlation tended to be better with absolute flow compared to relative uptake. The lower biases and RPC are due to 1) normalization of the relative uptake to a common scale and 2) avoidance of small rest values which amplify variation in stress/rest values. Thus the improved robustness of relative uptake comes at the expense of sensitivity to physiological global changes in blood flow as previously demonstrated [6].

Stress/Rest vs. Stress-Rest Differences

When using absolute flow, reproducibility of stress/rest was significantly worse than stress-rest as indicated by lower r^2 ($p<0.02$ for intra-operator 2, and $p<0.001$ for intra-operator 2 and inter-operator) and higher RPC values ($p<0.001$ for intra-operator 1, intra-operator 2, and inter-operator) as shown in Fig. 12 and Fig. 13 respectively. The reduced reproducibility of stress/rest is due to the higher sensitivity of the ratio to changes in low resting flow values, to which the subtraction operation in stress-rest is more robust. Thus, stress-rest measurements appear to be more reproducible than stress/rest, and therefore may be more sensitive to monitor serial changes. Both the stress-rest difference and ratio reflect the vasodilatory capacity to increase flow over baseline conditions. However, our results suggest that stress-rest is expected to be more robust, particularly in regions of infarction where low resting flow values may cause the stress/rest to appear artificially elevated.

When using relative uptake, a systematic difference between reproducibility of stress/rest and stress-rest was not observed. This is explained by the removal of small rest values through normalization of the rest (and stress) images.

Limitations

This study is limited by having two operators and two datasets each. Furthermore, a single operator represented novices and a single operator represented experts. However, we do feel that by having two operators at opposite ends of the spectrum of experience we are able to bound the actual operator variability that will be experienced in the majority of operator groups.

While this work did not address accuracy or test-retest reproducibility of our methods, previous studies addressed ^{82}Rb quantification accuracy [19] and diagnostic accuracy in 3-vessel disease [6].

Conclusion

The FlowQuant software program has been developed for reproducible quantification of myocardial blood flow and myocardial flow reserve using ^{82}Rb PET in routine practice and in clinical research. We have evaluated the intra- and inter-operator variability both for absolute flow quantification and for relative uptake analysis. We have demonstrated excellent agreement between both novice and expert operators; however, better reproducibility was

measured in the expert operator. To minimize variability, new operators must be trained using a small set of suitable cases and their performance should be tracked during the learning phase.

Appendix A

The spline optimization algorithm minimized a cost function, C_{energy}, that resulted in maximization of the image energy overlapping the spline model. Penalties were applied to discourage abnormal myocardial shapes by minimizing the following metrics:

1. Eccentricity of SA – the LV should be somewhat circular, thus if slices with a variation of radii greater than 30% exist, a penalty was applied.

$$C_{elip} = \begin{cases} 0 & e < 0.3 \\ e & e \geq 0.3 \end{cases} \qquad e = \max_i \left| \log(r_{hor_i}/r_{ver_i}) \right| \tag{6}$$

2. Relative size of atrium – the cross section of the atrium should not be bigger than that of the ventricle, thus a penalty was applied if the mean of its radii was more than 20% larger than the mean of the radii of the basal and cavity sections.

$$C_{atrium} = \begin{cases} 0 & a < 1.2 \\ a & a \geq 1.2 \end{cases} \qquad a = \frac{1}{2} \frac{r_{hor_{atrium}} + r_{ver_{atrium}}}{r_{hor_{cavity}} + r_{ver_{cavity}} + r_{hor_{base}} + r_{ver_{base}}} \tag{7}$$

3. Offset of center of ellipse from LV long axis - the LV myocardium should be nearly centered on the LV long axis, thus a penalty was applied if the center of the myocardium was displaced from the LV long axis by more than 40% of the mean radius in the same slice.

$$C_{offset} = \begin{cases} 0 & o < 0.4 \\ o & o \geq 0.4 \end{cases} \qquad o = \max_i \left[\frac{2o_i}{r_{ver_i} + r_{hor_i}} \right] \tag{8}$$

The final cost function, C, defined by equation (9) accounted for all the above penalties while rewarding for energy overlapping the LV model. Thus the LV model was constrained to have a characteristic shape, but abnormal myocardial shapes could be accommodated by the model, provided the image intensity is sufficient to offset the penalties.

$$C = C_{energy}(1 + 10 \times C_{elip} + C_{atrium} + C_{offset}) \tag{9}$$

References

[1] Thom T, Haase N, Rosamond W, Howard VJ, Rumsfeld J, Manolio T, et al. Heart disease and stroke statistics - 2006 update. Circ. 2006;113:e85-151.

[2] Murray CJ, Lopez AD. Global mortality, disability, and the contribution of risk factors: Global burden of disease study. Lancet 1997;349:1436-42.

[3] Gulati M, Pandey DK, Arnsdorf MF, Lauderdale DS, Thisted RA, Wicklund RH, et al. Exercise capacity and the risk of death in women. Circ. 2003;108:1554-9.

[4] Yoshida K, Mullani N, Gould KL. Coronary flow and flow reserve by PET simplified for clinical applications using rubidium-82 or nitrogen-13-ammonia. J Nucl Med. 1996;37:1701-12.

[5] Gould KL. Quantification of coronary artery stenosis in vivo. Circ Res. 1985;57:341-53.

[6] Parkash R, deKemp RA, Ruddy TD, Kitsikis A, Hart R, Beauschene L, et al. Potential utility of rubidium 82 PET quantification in patients with 3-vessel coronary artery disease. J Nucl Cardiol. 2004;11:440-9.

[7] Hutchins GD, Schwaiger M, Rosenspire KC, Krivokapich J, Schelbert H, Kuhl DE. Noninvasive quantification of regional blood flow in the human heart using N-13 ammonia and dynamic positron emission tomographic imaging. J Am Coll Cardiol. 1990;15:1032-42.

[8] Gerwitz H, Skopicki HA, Abraham SA, Castano H, Dinsmore RE, Alpert NM, et al. Quantitative PET measurements of regional myocardial blood flow: Observations in humans with ischemic heart disease. Cardiology 1997;88:62-70.

[9] Dayanikli F, Grambow D, Muzik O, Mosca L, Rubenfire M, Schwaiger M. Early detection of abnormal coronary flow reserve in asymptomatic men at high risk for coronary artery disease using positron emission tomography. Circ. 1994;90:808-17.

[10] Yoshinaga K, Tamaki N, Ruddy TD, deKemp RA, Beanlands RSB, Evaluation of Myocardial Perfusion. In: Wahl RL, editor. Principles and Practice of PET and PET/CT, 2nd ed. Philadelphia, PA, USA: Lippincott Williams & Wilkins; 2009. p. 541-64.

[11] Schindler TH, Nitzsche EU, Schelbert HR, Olschewski M, Sayre J, Mix M, et al. Positron emission tomography-measured abnormal responses of myocardial blood flow to sympathetic stimulation are associated with the risk of developing cardiovascular events. J Am Coll Cardiol. 2005;45:1505-12.

[12] deKemp RA, Ruddy TD, Hewitt T, Dalipaj MM, Beanlands RSB. Detection of serial changes in absolute myocardial perfusion with 82Rb PET. J Nucl Med. 2000;41:1426-35.

[13] Kaufmann PA, Camici PG. Myocardial blood flow measurements by PET: Technical aspects and clinical applications. J Nucl Med. 2005;46:75-88.

[14] Yoshinaga K, Chow BJW, Williams K, Chen L, deKemp RA, Garrard L, et al. What is the prognostic value of myocardial perfusion imaging using rubidium-82 positron emission tomography? J Am Coll Cardiol. 2006;48:1029-39.

[15] Tio RA, Dabeshlim A, Siebelink HMJ, de Sutter J, Hillege HL, Zeebregts CJ, et al. Comparison between the prognostic value of left ventricular function and myocardial perfusion reserve in patients with ischemic heart disease. J Nucl Med. 2009;50:214-9.

[16] Lautamäki R, George RT, Kitagawa K, Higuchi T, Merrill J, Voicu C, et al. Rubidium-82 PET-CT for quantitative assessment of myocardial blood flow: validation in a canine model of coronary artery stenosis. Eur J Nucl Med Mol Imaging. 2009;36:576-86.

[17] deKemp RA, Klein R, Renaud JM, Alghamdi A, Lortie M, DaSilva J, et al. 3D listmode cardiac PET for simultaneous quantification of myocardial blood flow and ventricular function. IEEE NSS-MIC Conference

Record 2008:5215-8.

[18] Lortie M, Beanlands RSB, Yoshinaga K, Klein R, DaSilva JN, deKemp RA. Quantification of myocardial blood flow with 82Rb dynamic PET imaging. Eur. J Nucl Med Mol. Imaging 2007;34:1765-74.

[19] Manabe O, Yoshinaga K, Katoh C, Naya M, deKemp RA, Tamaki N. Repeatability of rest and hyperemic myocardial blood flow measurements with 82Rb dynamic PET. J Nucl Med. 2009;50:68-71.

[20] Merhige ME, Breen WJ, Shelton V, Houston T, D'Arcy BJ, Perna AF. Impact of myocardial perfusion imaging with PET and (82)Rb on downstream invasive procedure utilization, costs, and outcomes in coronary disease management. J Nucl Med. 2007;48:1069-76.

[21] Alvarez-Diez TM, deKemp RA, Beanlands RS, Vincent J Manufacture of strontium-82/rubidium-82 generators and quality control of rubidium-82 chloride for myocardial perfusion imaging in patients using positron emission tomography. Appl Radiat Isot. 1999;50:1015-23.

[22] Klein R, Adler A, Beanlands RS, deKemp RA. Precision-controlled elution of a 82Sr/82Rb generator for cardiac perfusion imaging with positron emission tomography. Phys Med Biol. 2007;52:659-73.

[23] deKemp R, Klein R, Lortie M, Beanlands R. Constant-activity-rate infusions for myocardial blood flow quantification with 82Rb and 3D PET. IEEE NSS-MIC Conference Record 2006;6:3519-21.

[24] Lammertsma AA. Myocardial perfusion in 3 dimensions. J Nucl Med. 2002;48:1041-3.

[25] deKemp RA, Yoshinaga K, Beanlands RSB. Will 3-dimensional PET-CT enable the routine quantification of myocardial blood flow? J Nucl Cardiol. 2007;14:380-97.

[26] Buckberg GD, Luck JC, Payne DB, Hoffman JIE, Archie JP, Fixler DE. Some sources of error in measuring regional blood flow with radioactive microspheres. J Appl Physiology. 1971;31:598-604.

[27] Herrero P, Kim J, Sharp TL, Engelbach JA, Lewis JS, Gropler RJ, et al. Assessment of myocardial blood flow using 15O-water and 1-11C-acetate in rats with small-animal PET. J Nucl Med 2006;47:477-85.

[28] Mullani NA, Goldstein RA, Gould KL, Marani SK, Fisher DJ, O'Brien HA, et al. Myocardial perfusion with rubidium-82. I. Measurement of extraction fraction and flow with external detectors. J Nucl Med. 1983;24:898-906.

[29] DeGrado TR, Hanson MW, Turkington TG, Delong DM, Brezinski DA, Vallée JP, et al. Estimation of myocardial blood flow for longitudinal studies with 13N-labeled ammonia and positron emission tomography. J Nucl Med. 1996;3:494-507.

[30] El Fakhri G, Kardan A, Sitek A, Dorbala S, Abi-Hatem N, Lahoud Y, et al. Reproducibility and accuracy of quantitative myocardial blood flow assessment with 82Rb PET: Comparison with 13N-ammonia PET. J Nucl Med. 2009;50:1062-71.

[31] Chareonthaitawee P, Christenson SD, Anderson JL, Kemp BJ, Hodge DO, Ritman EL, et al. Reproducibility of measurements of regional myocardial blood flow in a model of coronary artery disease: Comparison of H2 15O and 13NH3 PET techniques. J Nucl Med. 2006;47:1193-1201.

[32] Scott NS, Le May MR, deKemp RA, Ruddy TD, Labinaz M, Marquis JF, et al. Evaluation of myocardial perfusion using rubidium-82 positron emission tomography after myocardial infarction in patients receiving primary stent implantation or thrombolytic therapy. Am J Cardiol. 2001;88:886-9.

[33] Sawada S, Muzik O, Beanlands RS, Wolfe E, Hutchins GD, Schwaiger M. Interobserver and interstudy variability of myocardial blood flow and flow-reserve measurements with nitrogen 13 ammonia-labeled positron emission tomography. J Nucl Med. 1995;2:413-22.

[34] Nagamachi S, Czernin J, Kim AS, Sun KT, Böttcher M, Phelps ME, et al. Reproducibility of measurements of regional resting and hyperemic myocardial blood flow assessed with PET. J Nucl Med. 1996;37:1626-31.

[35] Kaufmann PA, Gnecchi-Ruscone T, Yap JT, Rimoldi O, Camici PG. Assessment of reproducibility of baseline and hyperemic myocardial blood flow measurements with 15O-labeled water and PET. J Nucl Med. 1999;40:1848-56.

[36] Katoh C, Morita K, Shiga T, Kubo N, Nakada K, Tamaki N. Improvement of algorithm for quantification of regional myocardial blood flow using 15O-water with PET. J Nucl Med. 2004;45:1908-16.

[37] Jagathesan R, Kaufmann PA, Rosen SD, Rimoldi OE, Turkeimer F, Foale R, et al. Assessment of the long-term reproducibility of baseline and dobutamine-induced myocardial blood flow in patients with stable coronary artery disease. J Nucl Med. 2005;46:212-19.

[38] Wyss CA, Koepfli P, Mikolajczyk K, Burger C, von Schulthess GK, Kaufmann PA. Bicycle exercise stress in PET for assessment of coronary flow reserve - repeatability and comparison with adenosine stress. J Nucl Med. 2003;44:146-54.

[39] Nestrov SV, Han C, Mäki M, Kajander S, Naum AG, Helenius H, et al. Myocardial perfusion quantification with 15O-labeled water PET: high reproducibility of the new cardiac analysis software Carimas™). Eur J Nucl Med Mol Imaging. 2009;36:1594-1602.

[40] Knešaurek K, Machac J, Zhang Z. Repeatability of regional myocardial blood flow calculation in 82Rb PET imaging. BMC Med Phys. 2009;9:2.

[41] Schindler TH, Zhang XL, Prior JO, Cadenas J, Dahlbom M, Sayre J, et al. Assessment of intra- and interobserver reproducibility of rest and cold pressor test-stimulated myocardial blood flow with 13N-ammonia and PET. Eur J Nucl Med Mol Imaging. 2007;34:1178-88.

[42] Adachi I, Gaemperli O, Valenta I, Schepis T, Siegrist PT, Treyer V, et al. Assessment of myocardial perfusion by dynamic O-15-labeled water PET imaging: Validation of a new fast factor analysis. J Nucl Cardiol. 2007;14:698-705.

[43] Germano G, Kavanagh PB, Su HT, Mazzanti M, Kiat H, Hachamovitch R, et al. Automatic reorientation of three-dimensional, transaxial myocardial perfusion SPECT images. J Nucl Med. 1995;36:1107-14.

[44] PMOD Technologies. [Online].   http://www.pmod.com.

[45] Nekolla SG, Miethaner C, Nguyen N, Ziegler SI, Schwaiger M. Reproducibility of polar map generation and assessment of defect severity and extent in myocardial perfusion imaging using postiron emission tomography.

Eur J Nucl Med. 1998;25:1313-21.

[46] Dilsizian V, Bacharach SL, Beanlands RS, Bergmann SR, Delbeke D, Gropler RJ, et al. (2009, July) http://www.asnc.org.

[47] Gerwitz H, Fischman AJ, Abraham S, Gilson M, Strauss HW, Alpert NM. Positron emission tomographic measurements of absolute regional myocardial blood flow permits identification of nonviable myocardium in patients with chronic myocardial infarction. J Am Coll Cardiol. 1994;23:851-59.

[48] Renkin EM. Transport of potassium-42 from blood to tissue isolated mammalian skeletal muscles. Am J Physiol. 1959;197:1205-10.

[49] Crone C. Permeability of capillaries in various organs as determined by use of the indicator diffusion method. Acta Physiol Scand. 1963;58:292-305.

[50] Altman DG, Bland JM. Measurement in medicine: the analysis of method comparison studies. Statistician. 1983:307-17.

[51] Austin RE, Aldea GS, Coggins DL, Flynn AE, Hoffman JIE. Profound spatial heterogeneity of coronary reserve - discordance between patterns of resting and maximal myocardial blood flow. Circ Res. 1990;67:319-31.

[52] Chareonthaitawee P, Kaufmann PA, Rimoldi O, Camici PG. Heterogeneity of resting and hyperemic myocardial blood flow in healthy humans. Circ Res. 2001;50:151-61.

Table 1 – Characteristics of Study Population (n=30)

		Mean ± Standard Deviation			
Age	[yrs]	64.9±10.0			
Gender (Male)	[N (%)]	11 (37%)			
Normal*	[N (%)]	14 (47%)			
Single vessel disease*	[N (%)]	12 (40%)			
Multi-vessel disease*	[N (%)]	4 (13%)			
MBF (n=30)		Operator 1		Operator 2	
		Dataset 1	Dataset 2	Dataset 1	Dataset 2
Global rest MBF	[ml/min / g]	1.04±0.41	1.04±0.41	1.04±0.41	1.04±0.41
Global stress MBF	[ml/min / g]	2.24±0.92	2.25±0.92	2.25±0.92	2.25±0.92
Global MFR		2.40±1.20	2.40±1.08	2.41±1.21	2.43±1.21
Global ΔMBF	[ml/min / g]	1.20±0.80	1.21±0.79	1.21±0.80	1.22±0.80

* Based on interpretation of standard relative uptake MPI
p=NS for mean differences of all operator/analysis combinations
p=NS for standard-deviation differences of all operator/analysis combinations

Table 2 – Number of operator interventions per dataset (out of 60 images)												
		Orientation Stage										Segmentation Stage
		Position			Angle			Ellipse Size				
	Gut	TV Plane	TV	VLA	HLA	TV	VLA	HLA	TV	VLA	HLA	
Op1S1	18	4	0	0	0	0	0	0	0	0	0	5
Op1S2	6	0	0	4	0	0	1	0	0	2	0	4
Op2S1	4	0	0	0	0	0	0	0	0	0	0	1
Op2S2	4	0	0	2	0	0	0	0	0	1	0	1

TV – Transverse Plane
VLA – Vertical Long Axis Plane
HLA – Horizontal Long Axis Plane

Table 3 – Regional and global RPC for inter- and intra-operator agreement of absolute flow					
	Absolute (ml/min/g)			% (of mean MBF)		
	Intra-operator 1	Intra-operator 2	Inter-operator	Intra-operator 1	Intra-operator 2	Inter-operator
LAD	0.080	0.076	0.065	4.80%	4.52%	3.90%
RCA	0.095	0.049	0.061	6.08%	3.11%	3.88%
LCX	0.075	0.038	0.048	4.51%	2.29%	2.86%
Global	0.068	0.053	0.050	4.13%	3.22%	3.06%

	Klein et al. (Present study)	El Fakhri et al. [30‡]	Knesaurek et al. [40]	Schindler et al. [41]	Sawada et al. [33]	Adachi et al. [42]	Nesterov et al. [39]
Software Program	FlowQuant	GFADS	PMOD	n.a.	n.a.	n.a	Carimas™
Radiotracer	^{82}Rb	^{82}Rb	^{82}Rb	^{13}N-ammonia	^{13}N-ammonia	^{15}O-water	^{15}O-water
N	30	22	12	20	12	23	10
Population	Patients	Mixed	Normals	Mixed	Mixed	Normals	Patients
Myocardium Segments	3	3	16	1	5	16	4
Inter-operator Correlation (r^2)							
Rest MBF	0.994	0.827<ρ<0.935	n.a.	0.92	0.99	n.a.	n.a.
Stress MBF	0.999		n.a.	0.76		n.a.	n.a.
MFR	0.986		n.a.	n.a.	0.97	n.a.	n.a.
Intra-operator Correlation (r^2)							
Rest MBF	0.990 - 0.998	0.99	n.a.	n.a.	n.a.	0.712	≤0.986
Stress MBF	0.998 - 0.999		n.a.	n.a.	n.a.		
MFR	0.976 - 0.993	0.97	0.98	n.a.	n.a.	n.a.	n.a.
Inter-operator Reproducibility (RPC%)							
Rest MBF	6.1%	n.a.	n.a.	12.0%	~9%	n.a.	<15%
Stress MBF	2.3%	n.a.	n.a.	28.1%	~13%	n.a.	<15%
MFR	12.6%	n.a.	n.a.	n.a.	~27%	n.a.	n.a.
Intra-operator Reproducibility (RPC%)							
Rest MBF	3.7% - 8.0%	1.7 %	8.5 %	n.a.	n.a.	~73%	<50%
Stress MBF	3.0% - 3.8%	1.4 %	6.3 %	n.a.	n.a.		<20%
MFR	8.5% - 16.8%	2.8 %	10.6 %	n.a.	n.a.	n.a.	n.a.

n.a. – not available

r –Pearson correlation

ρ –Spearman correlation

† – computed from reported standard error estimates

‡ – means of 4 repeat results for each operator
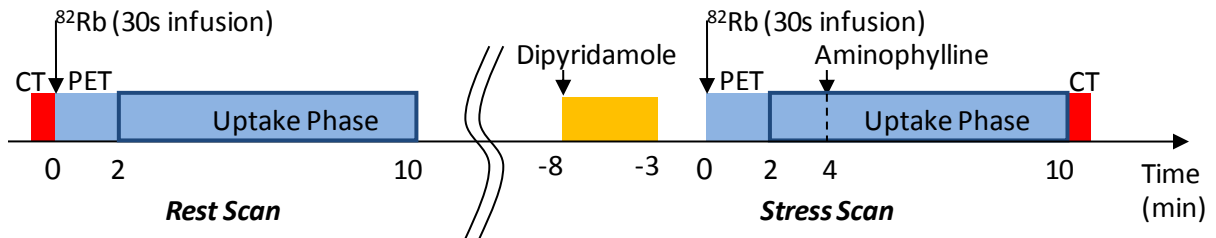
 – Estimated from reported results

Figures:

Fig. 1 – Clinical rest-stress ^{82}Rb PET/CT protocol using Dipyridamole pharmacologic stress.
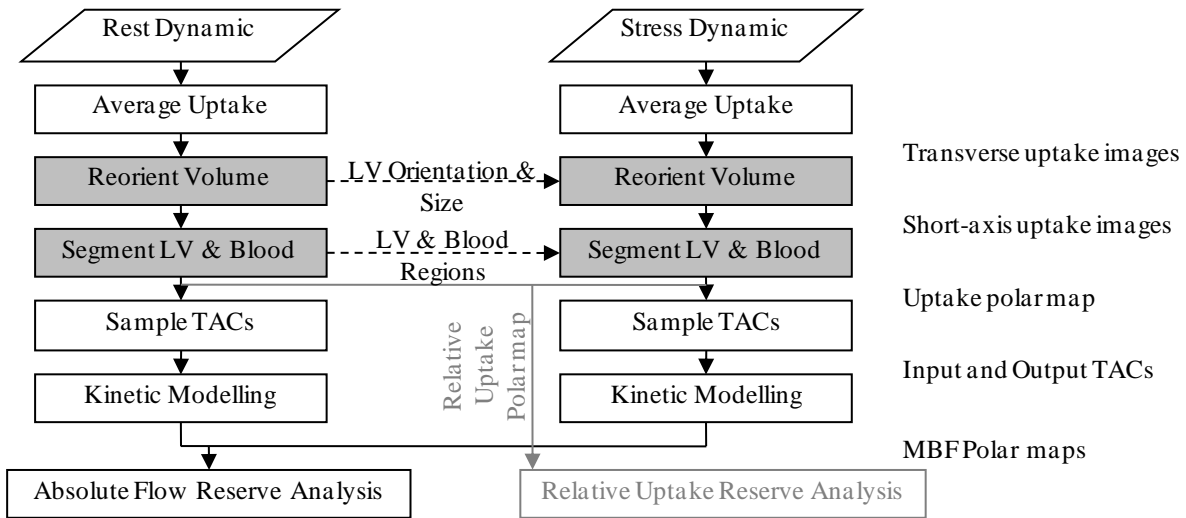

Fig. 2 – Dynamic ^{82}Rb rest-stress analysis workflow. Rest and stress dynamic images are used to generate relative uptake, absolute MBF, and flow reserve polar maps. The process is fully automated, with some user interaction possible at the reorientation and segmentation stages (gray filled boxes).
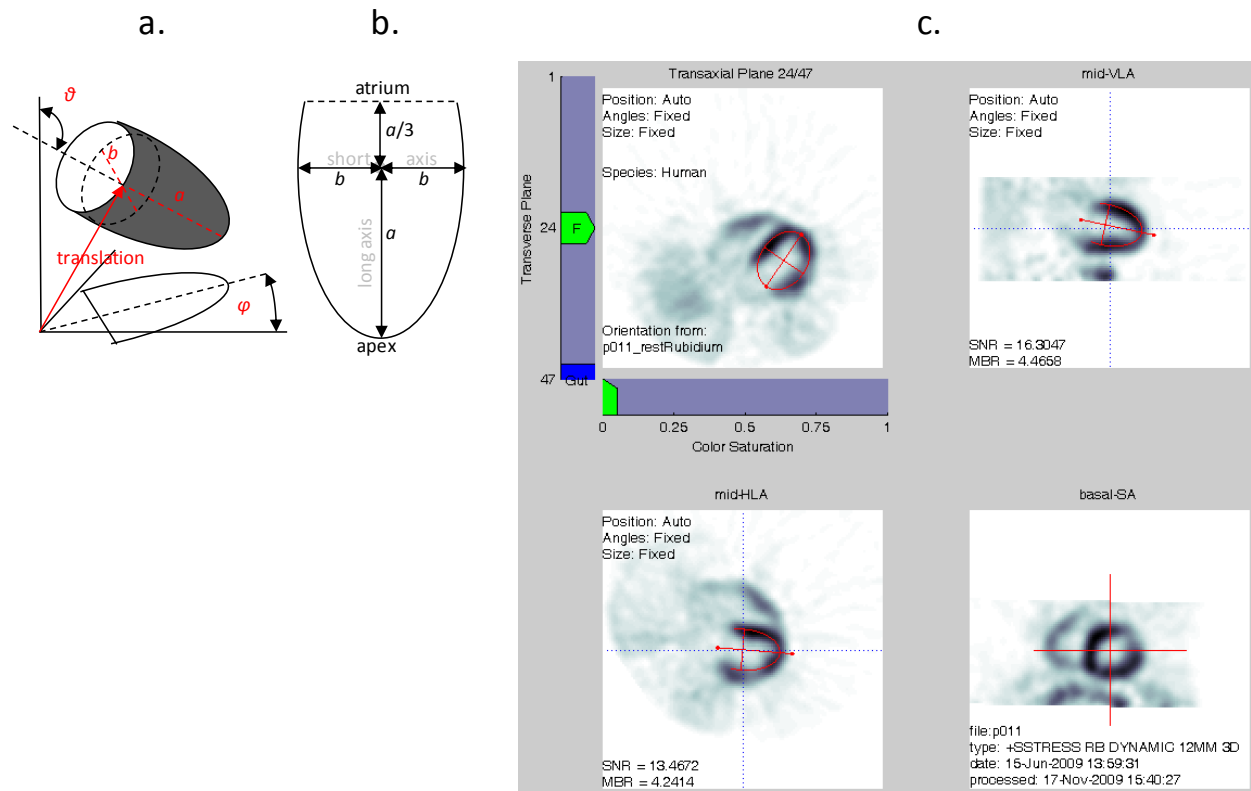
Fig. 3 – A. LV ellipse model and orientation in relation to the scanner reference frame. The axial angle φ and the sagittal angle θ describe the orientation in 3D. B. Partial ellipse used to model a mid-VLA cross-section. The ellipse dimensions are *a* and *b* along the long and short axes respectively. C. Automatic orientation GUI.
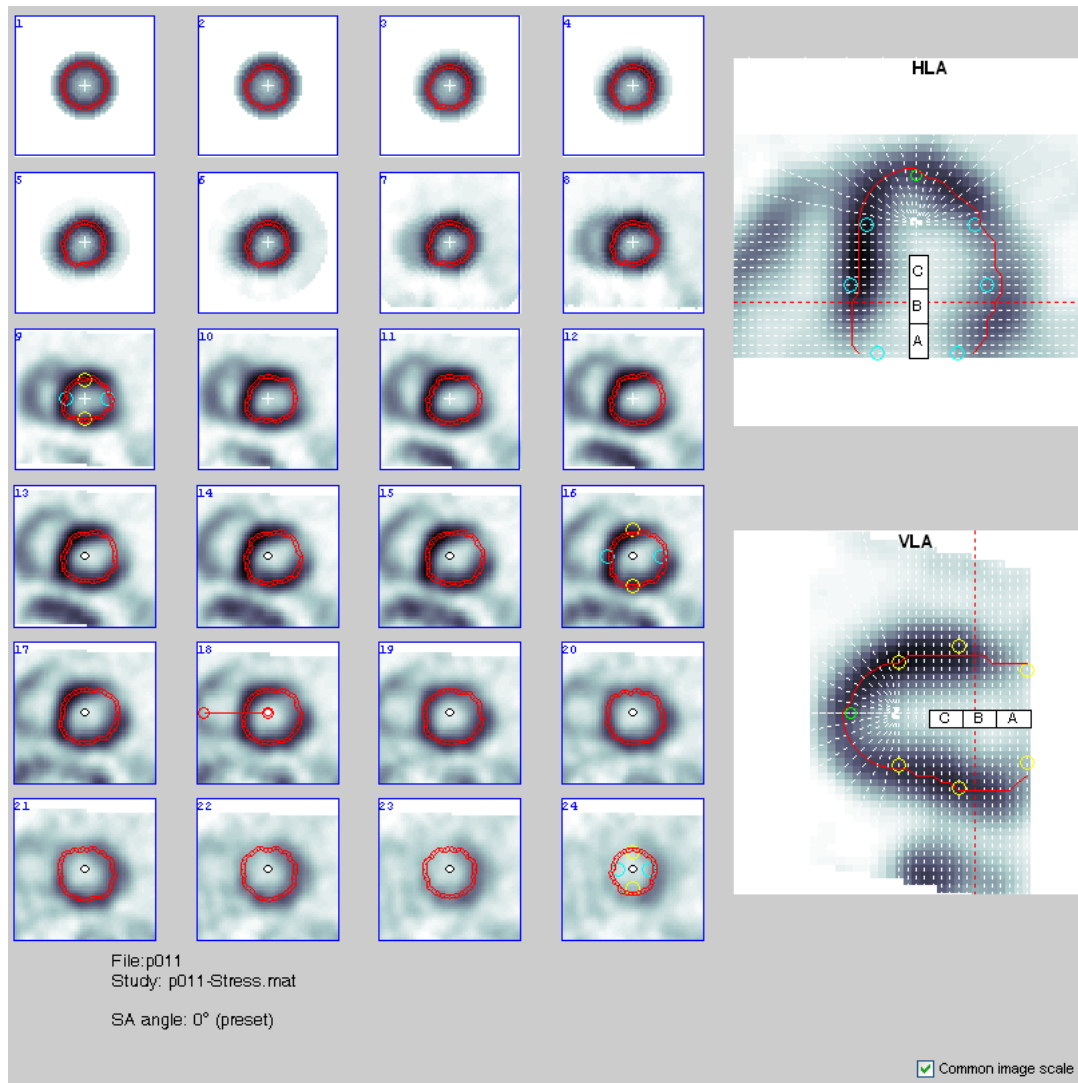
Fig. 4 – Myocardial segmentation on conical (1-9) and planar (10-24) slices of the same case as in Fig. 3c. Vertical and horizontal long axis slices are also shown on the right, with the dashed lines depicting the locations of the slices to the left. The red contour lines show the myocardial sampling regions, and the yellow and cyan circles are the spline model control points. The white crosses indicate the long axis and the black circles indicate the blood ROIs.
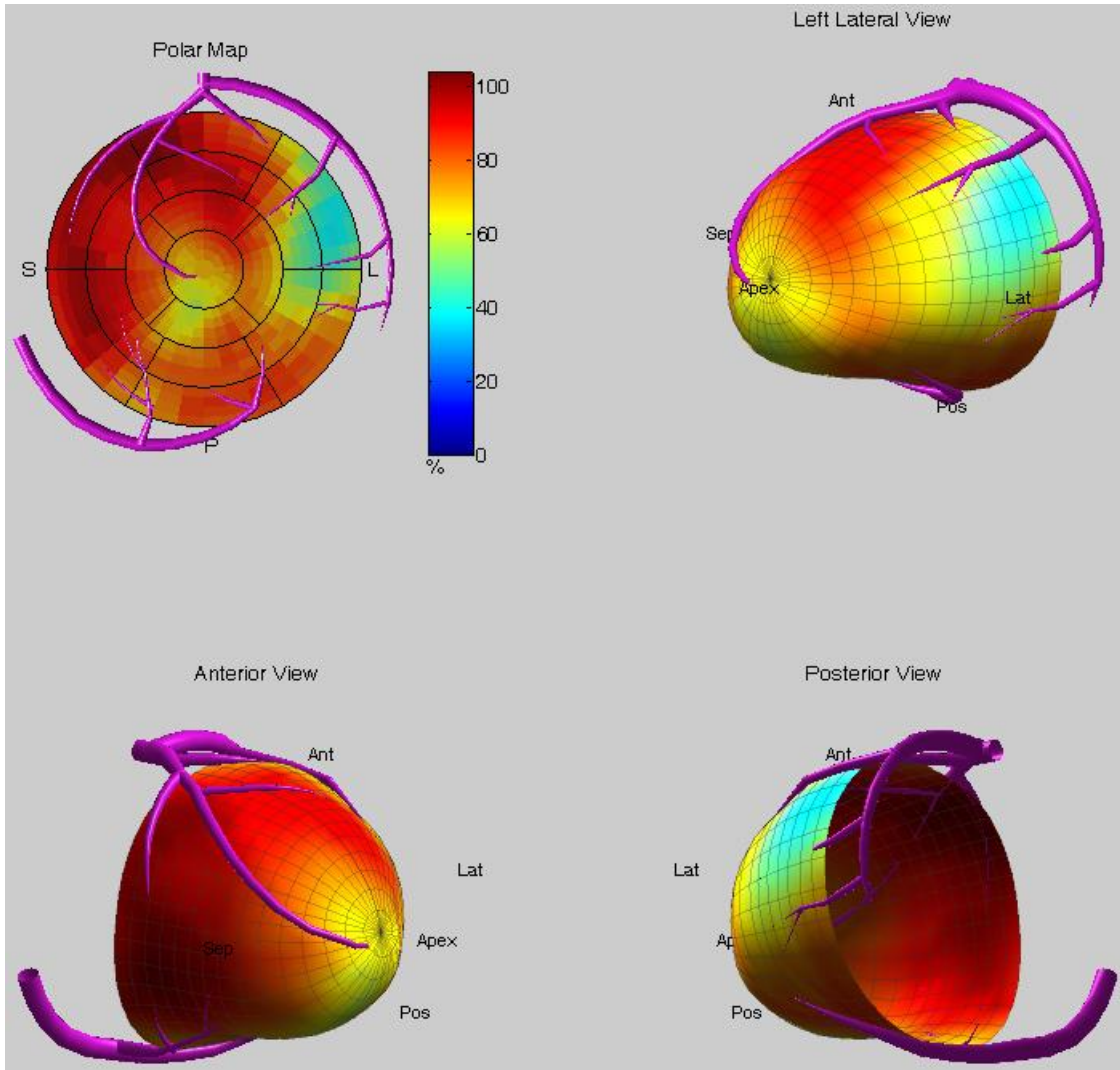
Fig. 5 – Polar map (top left) and 3D perspective views of the LV from different angles for the same case as in Fig. 3c and Fig 4. Model coronary arteries are superimposed to relate polar-map regions to the three main vascular territories.
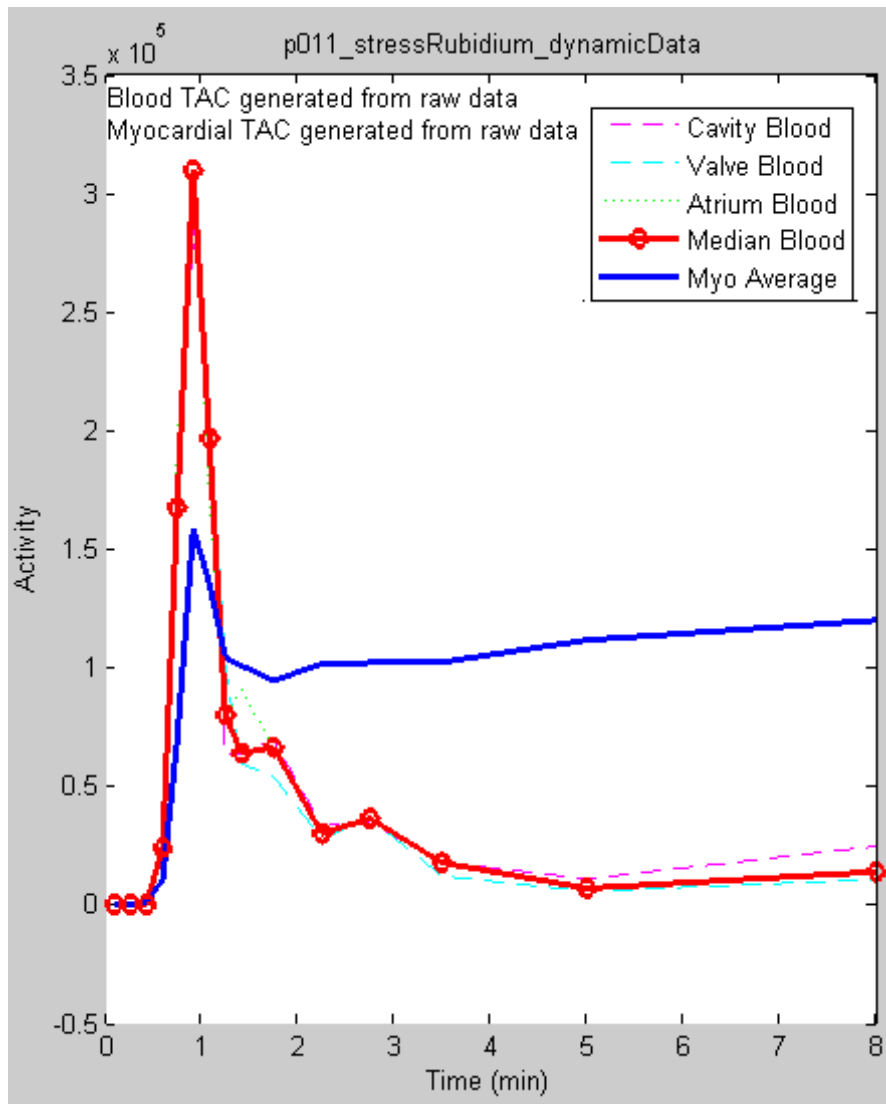
Fig. 6 – Time-activity-curves (TAC) for blood in three regions and their median (thick red) as well as the mean TAC for the myocardium region (blue) for the same case as in Fig. 3c and Fig. 4.
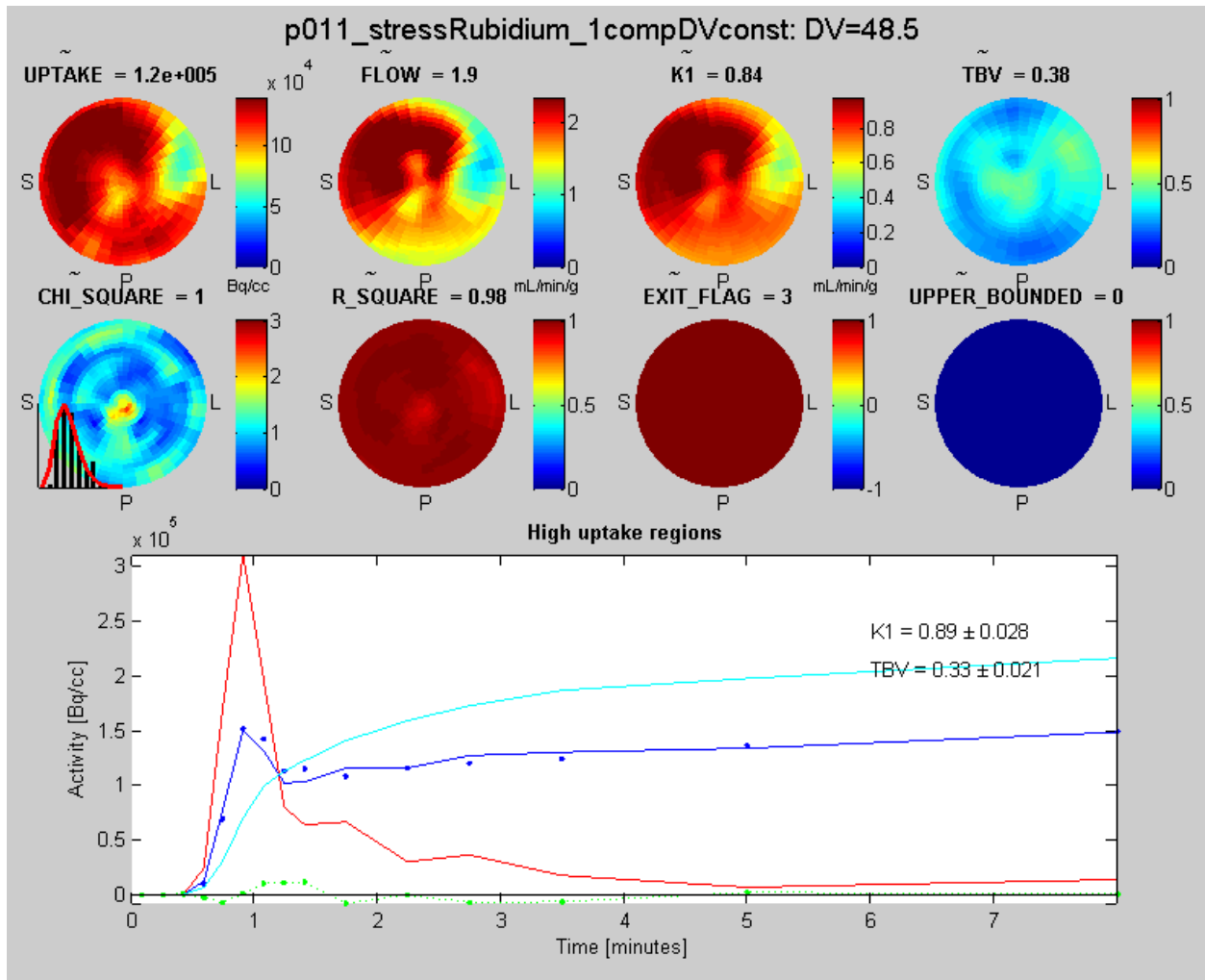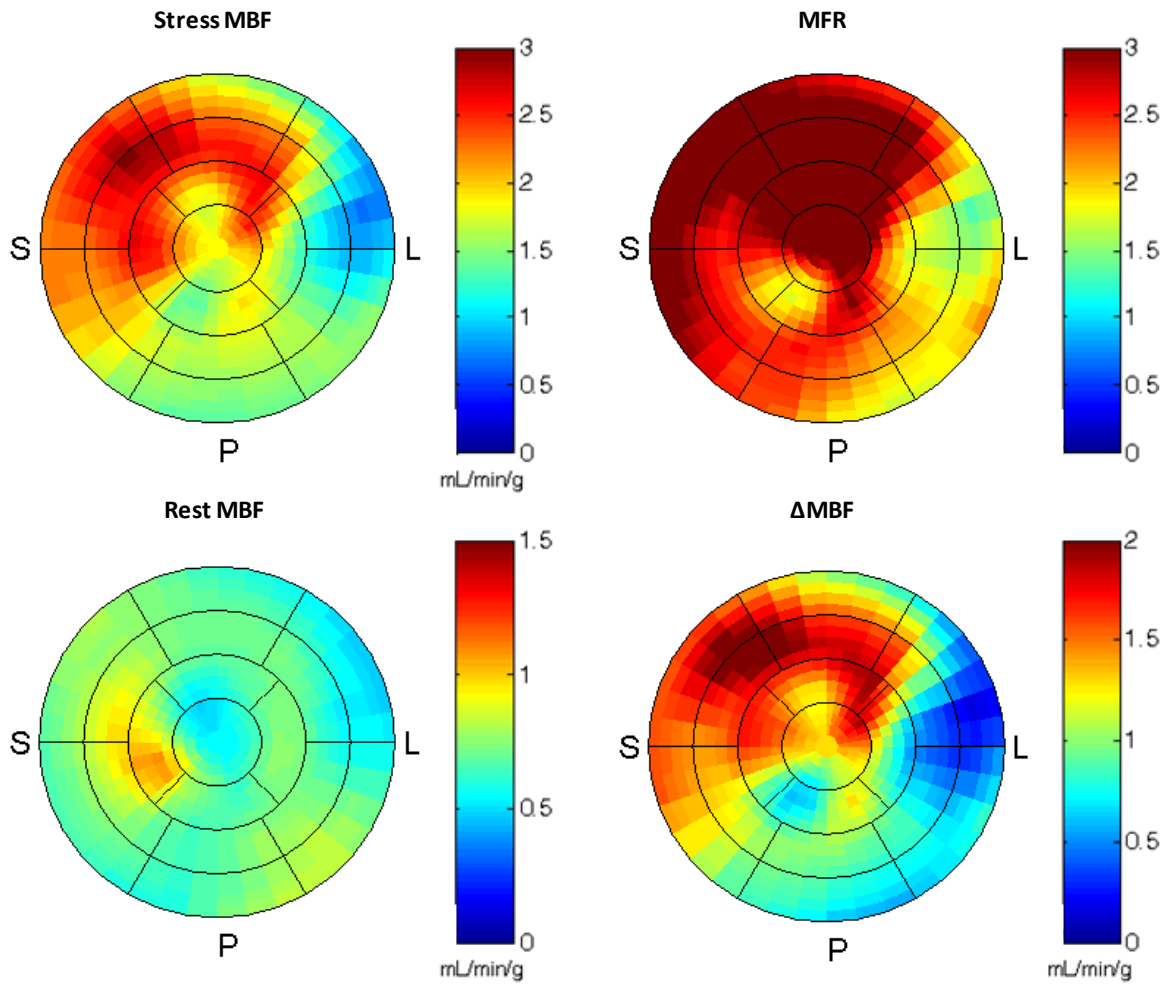
Fig. 7 – Kinetic modeling report for the same case as in Figures 3-6.

Fig. 8 – MBF, MFR, and ΔMBF analysis report with the rest case shown in Figures 3-7 indicates uniform rest and stress flows with MFR≈3.1 and ΔMBF≈2.2 mL/min/g, which indicate normal MBF. This case was interpreted as normal using relative uptake images (not shown).
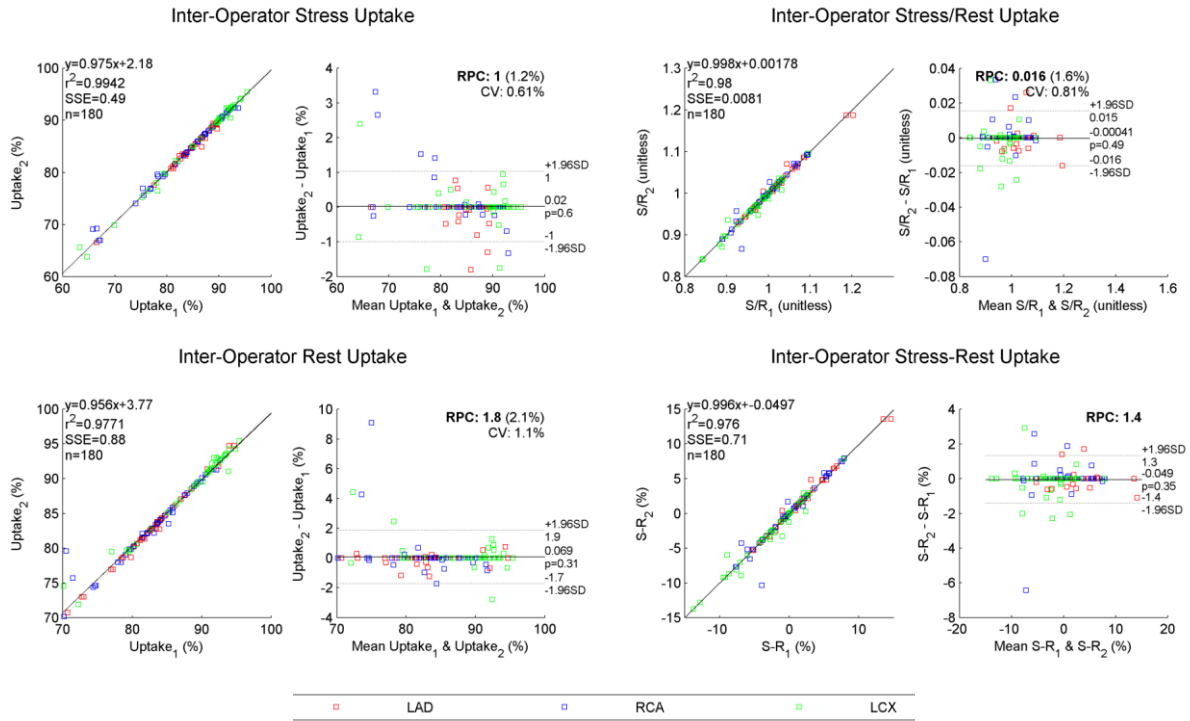
Fig. 9 – Bland-Altman graphs for inter-operator agreement of rest uptake, stress uptake, stress/rest uptake, and stress-rest (datasets 1 and 2 combined).
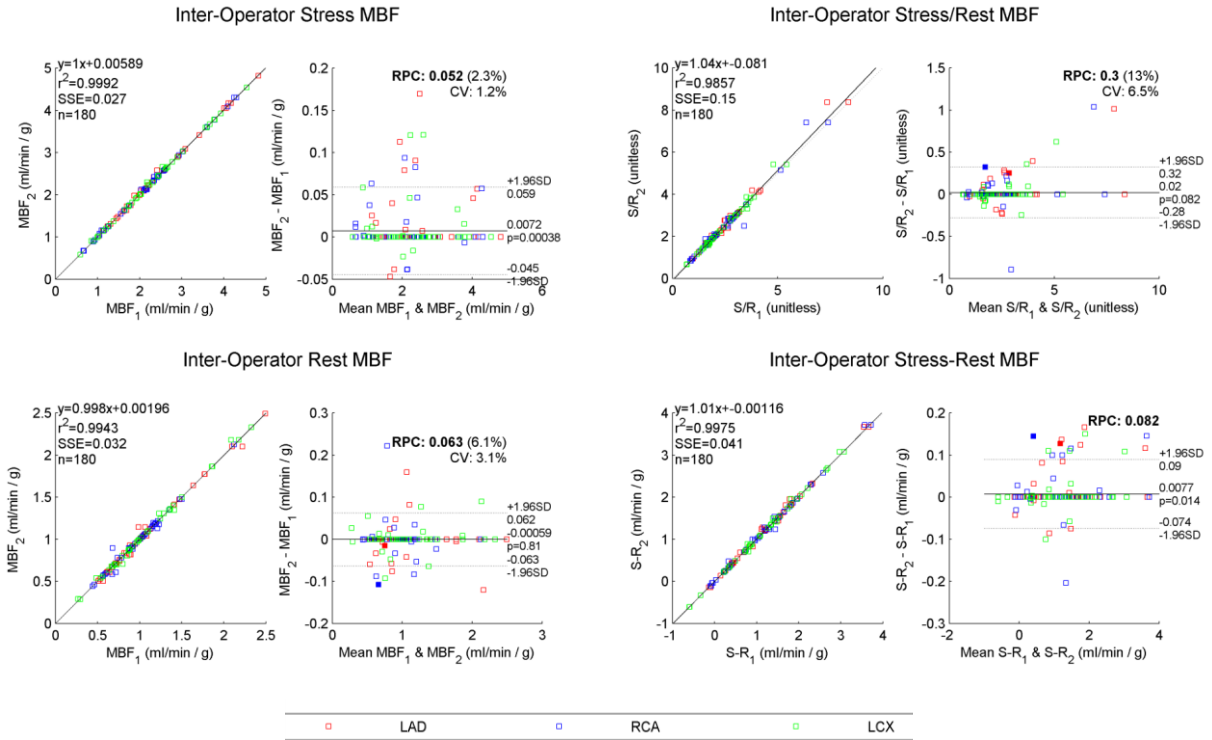
Fig. 10 – Bland-Altman graphs for inter-operator agreement of MBF, stress/rest MBF, and stress-rest MBF (datasets 1 and 2 combined).
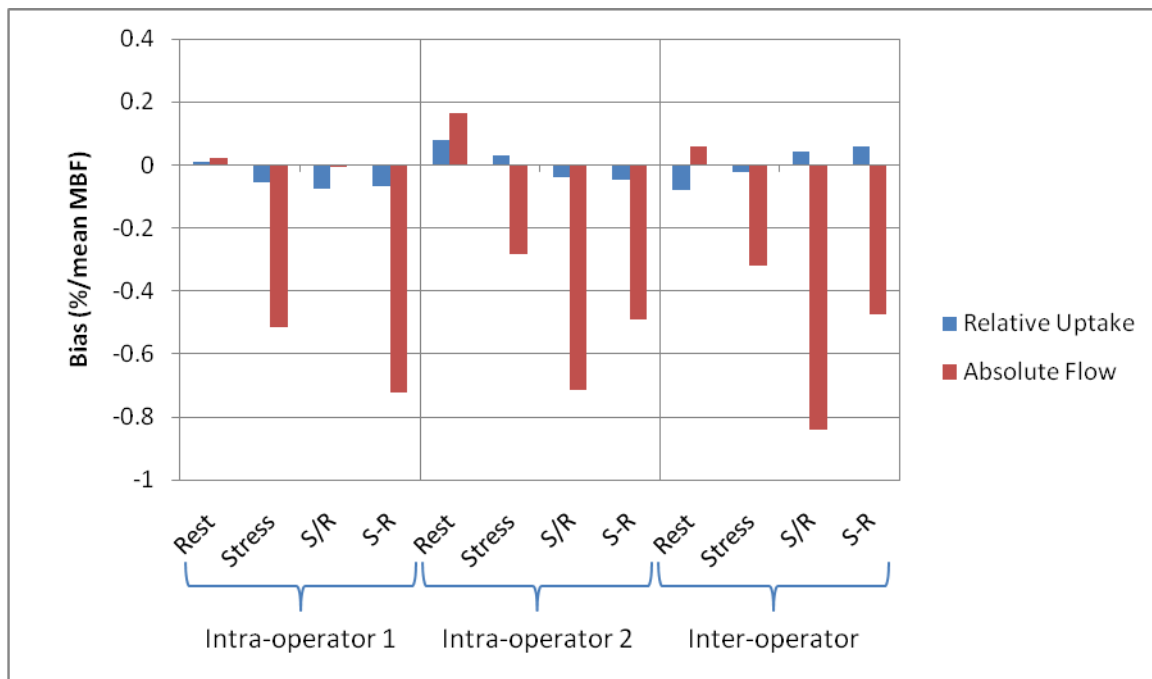

Fig. 11 – Biases in intra- and inter-operator agreement of relative uptake and absolute flow. All biases were not significantly different from zero (p>0.05) and remained below 1%.
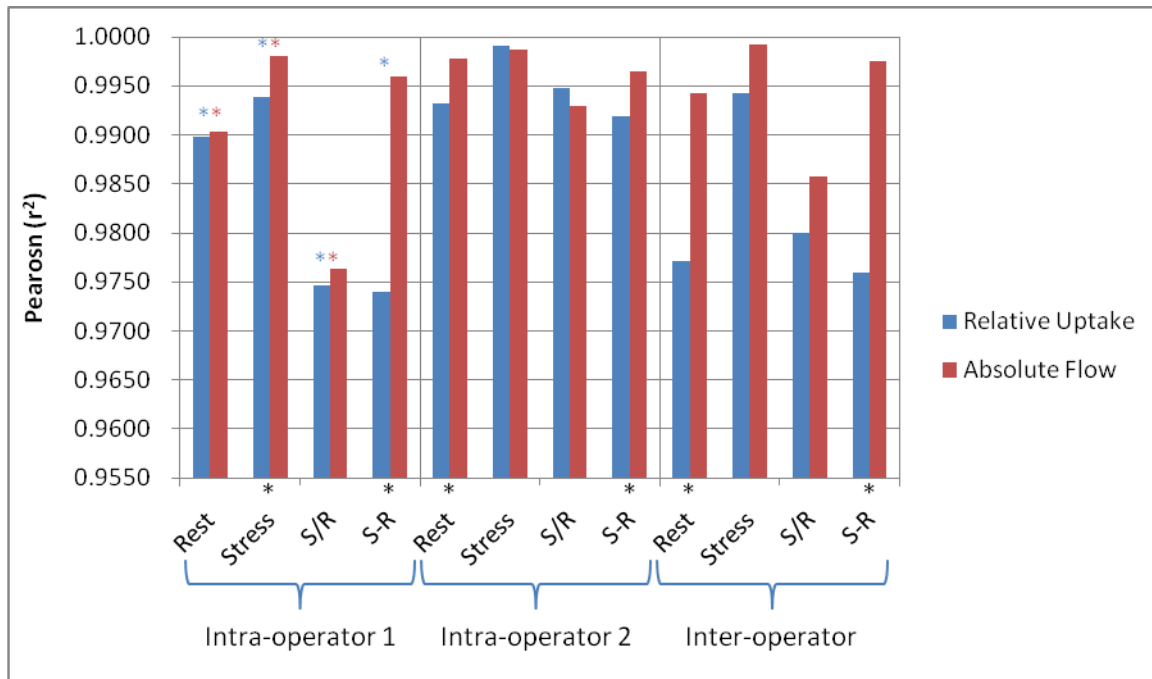
Fig. 12 – Pearson correlation (r^2) for intra- and inter-operator agreement of relative uptake and absolute flow. Operator 2 (experienced) had slightly higher agreement than operator 1 (novice) both with relative uptake (blue *) and absolute flow (red *). Absolute flow generally had better agreement than relative uptake, but was significant in only 6/12 comparisons (black *). Note the y-axis scale set to emphasize difference between data.
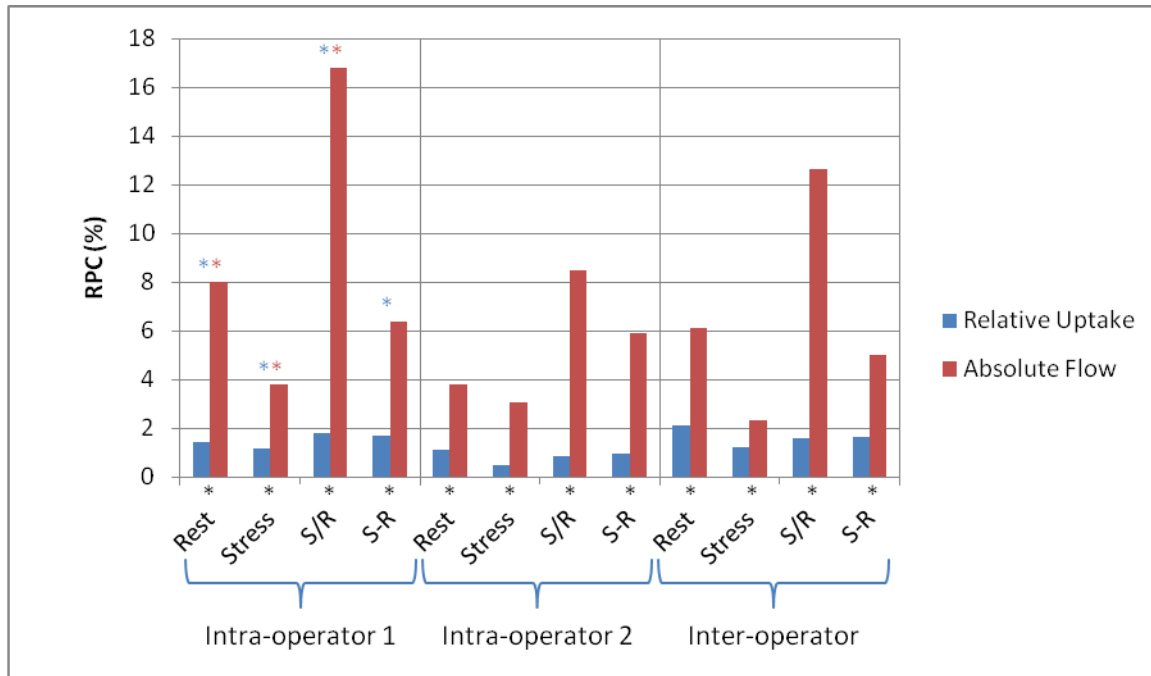
Fig. 13 – RPC for intra- and inter-operator differences of relative uptake and absolute flow. In all cases relative uptake analysis is less variable than absolute flow (p<0.001) (black *). Generally, operator 2 (experienced) had less variability than operator 1 (novice) for relative uptake (blue *) and absolute flow (red *).
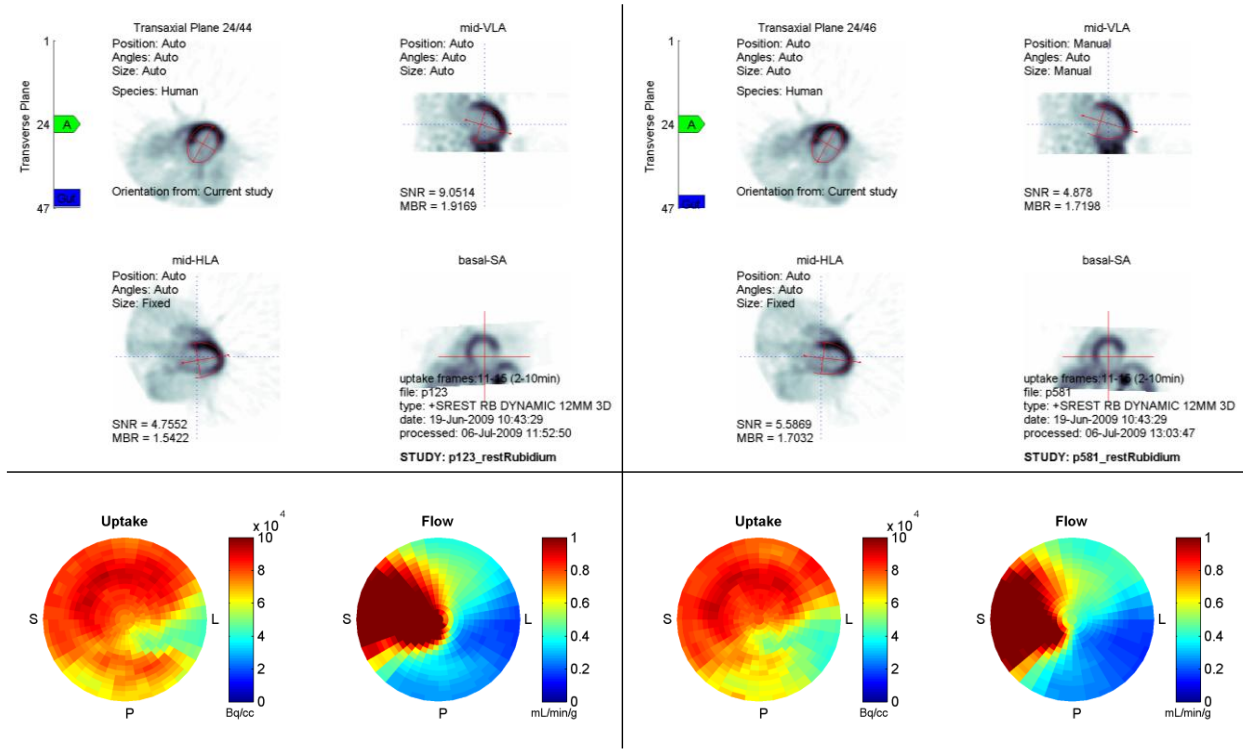
Fig. 14 – Example of analysis with the largest MBF discordance (intra-operator and inter-operator) demonstrating that the operator failed to correct for suboptimal detection of the LV in the mid-VLA (left) but did intervene in the second dataset (right). Similar orientations were copied to stress without further intervention. Consequently, the stress/rest and stress-rest maps differed mainly in scale, but less in spatial distribution.